PAPER

CrossMark
click for updates

Ferric carbide nanocrystals encapsulated in nitrogen-doped carbon nanotubes as an outstanding environmental catalyst†

Chen Wang,[a] Jian Kang,[a] Ping Liang,[a] Huayang Zhang,[a] Hongqi Sun,*[b] Moses O. Tadé[a] and Shaobin Wang*[a]

Nitrogen-doped carbon nanotubes encapsulating iron carbide (Fe_3C) nanocrystals (Fe_3C@NCNT) were fabricated by a simple and direct pyrolysis method using melamine and ferric chloride as the C, N and Fe precursors. The surface morphology, structure and composition of the Fe_3C@NCNT materials were thoroughly investigated. The nanomaterials were employed as novel catalysts for peroxymonosulfate (PMS) activation; outstanding efficiency, high stability and excellent reusability were observed in the catalytic oxidation of organics. The encapsulated Fe_3C nanoparticles played a key role in the emerging synergetic effects of the carbide and the protective graphitic layers. In addition, the quaternary N and trace amounts of iron on the CNT surface acted as the active sites. Various quenching experiments were carried out to elucidate the catalytic mechanism of Fe_3C@NCNT. It was found that singlet oxygen, superoxide, sulfate and hydroxyl radicals worked together to degrade phenol solutions. Due to their simple synthesis method, low-cost precursors, unique structure and excellent catalytic activity and stability, these novel iron-carbide-based composites have great potential as new strategic materials for environmental catalysis.

Environmental significance

Environmental contaminants caused by industrialization and urbanization, such as phenolics, are currently of great public concern because of their toxicity and resistance to natural degradation. Most homogeneous and heterogeneous catalytic processes are based on either noble, transition, or rare-earth metals or their oxides. A series of problems, such as scarcity, high cost and secondary pollution, have limited the wide applications of these catalysts. Therefore, novel carbon-based metal or metal-free catalysts that demonstrate both good catalytic performance and excellent stability are highly desirable. In this paper, nitrogen-doped carbon nanotubes with encapsulated iron carbide nanocrystals (Fe_3C@NCNT) were synthesized by simple and direct pyrolysis of melamine and ferric chloride. SEM and TEM revealed peapod-like structures with Fe_3C nanocrystals in the interior of the carbon nanotubes. Fe_3C@NCNT-900 completely degraded phenol in only 20 min and demonstrated superior stability. It was proven that the doped N (mainly quaternary N), inner Fe_3C, and trace amounts of Fe on the surface of the nanotubes were the active sites for catalytic performance. Different quenching experiments demonstrated that singlet oxygen, superoxide, sulfate and hydroxyl radicals worked together to degrade phenol solutions. This study opens a new avenue for the development of carbon-based metal catalysts and advances their application in wastewater remediation.

Introduction

The 21st century has been called the Century of the Environment.[1] Civilization and industrialization have resulted in the discharge of vast amounts of pollutants into water resources, with severe health and environmental implications.[2–6] Advanced oxidation processes (AOPs) combined with other physical processes, such as adsorption, extraction and flocculation, have been effectively applied for complete removal of these organic contaminants in wastewater. Metal-based materials, such as Co and Mn oxides,[7–10] are highly favorable to activate peroxymonosulfate (PMS) and produce sulfate radicals, thus facilitating emerging sulfate radical-based advanced oxidation processes (SR AOPs). However, these metal-based catalysts are subject to inevitable loss or leaching of metal ions in either homogeneous or heterogeneous reactions; thus, they cause secondary contamination.[11–14] Therefore, much effort has been devoted to developing carbon-based catalysts (M–N_x/C, M = Co, Fe, Ni, *etc.*), metal-free carbon materials and N-doped carbon catalysts (N_xC) as

a Department of Chemical Engineering and CRC for Contamination Assessment and Remediation of the Environment (CRC CARE), Curtin University, GPO Box U1987, Western Australia, Australia. E-mail: shaobin.wang@curtin.edu.au
b School of Engineering, Edith Cowan University, 270 Joondalup Drive, Joondalup, WA 6027, Australia. E-mail: h.sun@ecu.edu.au

alternatives to metal oxide catalysts.[15–17] Among these, M–N$_x$/C catalysts have emerged as superior candidates; their active sites are believed to arise from surface nitrogen coordinated with metals.[15,18] Although they have been extensively studied, these materials still suffer from either low catalytic activity or poor stability.[6,8,11,19,20] Therefore, it is very challenging to develop novel catalysts with high activity, good stability, low cost and environmental friendliness.

Fe-based materials are regarded as one of the most promising heterogeneous catalysts because Fe can be easily incorporated into carbon frameworks by pyrolyzing ferric salt in an inert atmosphere and can catalyze the graphitization process at lower temperatures.[21,22] In addition, metal-based catalysts coated by a protective shell or matrix have been proven to have enhanced catalytic performance and stability. Recently, novel and efficient metal/metal carbide nanoparticles encapsulated in nanostructured carbon were developed; their active sites are believed to be the graphitic carbon shells activated by the encapsulated nanoparticles.[23,24] An interesting magnetic carbon-encapsulated nano Fe^0/Fe$_3$C catalyst was synthesized by Wang et al.[25] via in situ hydrothermal carbonization of glucose with melamine accompanied by self-reduction in N$_2$ atmosphere. Its excellent catalytic performance was evidenced by the complete removal of 20 ppm phenol within 10 min. They found that the presence of Fe$_3$C was conducive to the stability of the catalyst. In addition, Li et al.[24] discovered a novel catalyst consisting of iron carbide nanoparticles encapsulated by graphitic layers and applied it to the oxygen reduction reaction (ORR). Bao et al.[23] prepared peapod-like carbon nanotubes with encapsulated Fe nanoparticles and used the materials as ORR catalysts in acid media. Peng et al.[26] synthesized nitrogen-doped carbon nanotubes with encapsulated Fe$_3$C nanoparticles that showed good ORR nature in both acid and alkaline media. Yao et al.[27] fabricated magnetic metal (M = Fe, Co, Ni) nanocrystals encapsulated in nitrogen-doped carbon nanotubes using dicyandiamide as a C/N precursor; these exhibited varying activities toward Fenton-like reactions. These findings are notable because the Fe$_3$C/Fe particles could 'etch' into the CNTs in situ, and the resulting iron species encapsulated inside CNTs or graphene are particularly active for selective hydrogenation[28] and the oxygen reduction reaction.[29,30] These important achievements inspired us to explore a new strategy for the controlled synthesis of novel carbon-supported iron-based catalysts for PMS activation with both high catalytic activity and excellent stability.

Carbon-based materials, such as carbon nanotubes (CNTs), have been extensively studied in both fundamental research and practical applications because of their unique physico-chemical properties. Heteroatom doping with nitrogen or metals can further tune and improve the capabilities of CNTs.[31] Melamine, a green and cheap chemical with 67 wt% N content, has been employed as both a carburization reagent and nitridation reagent.[32,33] Nallathambi et al. reported that the performance of Fe catalyst prepared from melamine was far superior to those of bipyridine, pyrazine and purine with the same N loading.[34] Single-walled NCNTs were synthesized by Duan et al. via the pyrolysis of commercial SWCNTs and melamine; these showed extraordinarily high catalytic activity for PMS activation.[35] However, a simple, low-cost, safe and scalable synthesis method of CNTs for the widespread and sustainable use of carbon materials on a large scale has been difficult to achieve.[28]

Generally, N-doped CNTs can be prepared through post-treatment of CNTs with ammonia, urea, or pyridine. However, there are few studies of the direct synthesis of N-doped CNTs from direct thermal carbonization of nitrogen-containing polymer precursors, such as polyacrylonitrile, polyaniline, polypyrrole, and melamine resin.[36,37] The in situ approach provides several advantages, such as an increase of the doping level and a uniform distribution of heteroatoms on CNTs, for improving catalytic activity. Furthermore, it has been concluded that encapsulation of metal nanocrystals into N-doped CNTs to form a hybrid structure is an effective strategy to enhance overall catalytic activity.[38,39]

Herein, we report a new, facile one-pot strategy for the controlled synthesis of N-doped carbon nanotubes with encapsulated Fe$_3$C through the direct pyrolysis of a mixture of melamine and iron chloride. Fe$_3$C and CNTs were formed in situ during pyrolysis. Their morphologies, compositions, active sites and mechanisms of catalytic degradation were systematically investigated. In addition, electron paramagnetic resonance (EPR) and classical radical quenching tests were used to probe PMS activation and the mechanism of phenol oxidation. To our best knowledge, this is the first report of well-designed Fe$_3$C-based CNTs composites with great potential for catalytic activity and good stability for PMS reactions.

Experimental

Materials and chemicals

Melamine (>99.0%), hexahydrate ferric chloride (FeCl$_3$·6H$_2$O, >99.9%), potassium peroxymonosulfate (2KHSO$_5$·3KHSO$_4$·K$_2$SO$_4$, oxone), sodium azide (NaN$_3$), p-benzoquinone (PBQ), tert-butyl alcohol (TBA) and 5,5-dimethylpyrroline-oxide (DMPO, >99.0%) were purchased from Sigma-Aldrich. Phenol (>99.0%), acetone, ethanol and hydrochloric acid (32% to 37%) were obtained from Chem-Supply. High purity nitrogen gas (99.999%) was obtained from BOC. Ultrapure water was used in all of the experiments. All chemicals used herein were of analytic grade and were used as received without any further purification.

Synthesis of Fe$_3$C@NCNT

Fe$_3$C@NCNT catalysts were fabricated via a facile thermal process using melamine as a C/N precursor.[6,26,40] In a typical procedure, 6 g melamine and 6 g FeCl$_3$·6H$_2$O were dissolved in 10 mL ethanol in a crucible with continuous stirring to form a clear yellow solution. The resulting solution was then placed in an oven at 80 °C in air for around 48 h to afford a tawny solid. The dried powder was transferred to a quartz tube furnace to respectively anneal at 700 °C, 800 °C, or 900

This journal is © The Royal Society of Chemistry 2017

Environ. Sci.: Nano, 2017, 4, 170–179 | 171

°C for 6 h under a nitrogen flow of 50 mL min^{-1}. After cooling to room temperature, the as-obtained material was treated with 100 mL hydrochloric acid (32 to 37 wt%) with magnetic stirring for 6 h to remove any accessible iron species. The sample was then washed successively with ultrapure water and acetone and dried at 60 °C for 24 h to obtain the final material, named Fe$_3$C@NCNT-X (X indicates the pyrolysis temperature). The obtained products were magnetic powders (ESI,† Fig. S1). A schematic of the synthesis route of the Fe$_3$C@NCNT catalysts is illustrated in Fig. 1(a).

Characterization of materials

X-ray diffraction (XRD) patterns were acquired on a Bruker D8-Advanced X-ray instrument using Cu-Kα radiation with λ at 1.5418 Å. Scanning electron microscopy (SEM) was applied to investigate the morphologies of the catalysts using a Zeiss Neon 40 EsB FIBSEM. Nitrogen sorption isotherms were acquired on a Tristar II 3020 instrument after degassing the samples for 4 h at 100 °C. The specific surface area and pore size distribution were evaluated by the Brunauer–Emmett–Teller (BET) equation and the Barrett–Joyner–Halenda (BJH) method, respectively. The chemical compositions and states of the catalysts were determined by X-ray photoelectron spectroscopy (XPS), which was carried out on a Thermo Escalab 250 instrument with Al-Kα X-rays. A Perkin-Elmer Diamond TGA/DTA thermal analyzer was utilized to perform thermogravimetric-differential thermal analysis (TG-DTA) *via* heating the samples in an air flow of 100 mL min^{-1} at a heating rate of 10 °C min^{-1}. Raman analysis was performed using an ISA dispersive Raman spectrometer with an argon ion laser (514 nm). The detection of iron ions after phenol degradation was performed on an Optima 8300 ICP-OES spectrometer (PerkinElmer). The samples were also subjected to ultimate analysis using an elemental analyzer (Perkin-Elmer 2400 SeriesIImodel).

Catalytic oxidation of phenol solutions

The catalytic oxidation was carried out in a 250 mL conical flask with phenol solution (20 ppm, 150 mL), the catalyst (0.2 g L^{-1}) and PMS (2.0 g L^{-1}) in a constant-temperature (25 °C) controlled water bath for the kinetic studies. During each interval, 1 mL phenol solution was withdrawn with a syringe, filtered with a 0.45 μm Millipore film, and injected into a vial in which 0.5 mL of methanol as a quenching reagent had been previously injected. The mixed solution was analyzed using a high performance liquid chromatograph (HPLC, Varian) with a C-18 column and a UV detector set at 270 nm. After each run, the used catalyst was collected by ultrasonic washing for 5 min, washed three times with ultrapure water, filtered and dried in an oven for reuse.

Mechanistic studies of the catalytic processes

An EMS-plus EPR instrument from Bruker was employed to detect the free radicals captured by 5,5-dimethyl-1-pyrroline (DMPO, >99.0%) during PMS activation, operating under the following conditions: centre field, 3515 G; sweep width, 100 G; microwave frequency, 9.87 GHz; power setting, 18.75 mW; scan number, 3. Quantitative information regarding the radicals was acquired using the SpinFit software in the Bruker Xenon Software Package.

Results and discussion

Characterization of Fe$_3$C@NCNT

The morphologies and structures of as-prepared Fe$_3$C@NCNT-700, Fe$_3$C@NCNT-800 and Fe$_3$C@NCNT-900 are shown in Fig. 1b–d and Fig. S2 (ESI†). The characteristic morphologies of all the catalysts were dimensionally uniform and orderly arranged nanotubes with diameters of 200 to 300 nm for Fe$_3$C@NCNT-700 and Fe$_3$C@NCNT-800 but only 50 to 100 nm for Fe$_3$C@NCNT-900.[26,28] However, CNTs with nonuniform sizes with significant agglomeration were formed above 900 °C, which may be attributed to the breakdown of the CNTs and decomposition of Fe$_3$C at higher temperatures.

As revealed by transmission electron microscopy (TEM) images (Fig. 2), a large portion of pea-pod dark nanocrystals (identified as iron carbide by the XRD diffraction patterns, Fig. 3) were mainly encapsulated inside the channels or at the tips of the carbon nanotubes (sized 40 to 50 nm for Fe$_3$C@NCNT-700 and Fe$_3$C@NCNT-900 and 80 to 100 nm for Fe$_3$C@NCNT-800). HRTEM images of the Fe$_3$C nanoparticles in CNTs show that most of the surfaces of the Fe$_3$C nanoparticles were coated with multi-layered graphene. For a typical nanoparticle, the spacing of crystalline lattices in one direction was 0.31 nm, corresponding to the (111) crystal plane of Fe$_3$C phase. The interlayer spacing of the coating graphene layer was 0.335 nm, in accordance with the experimental
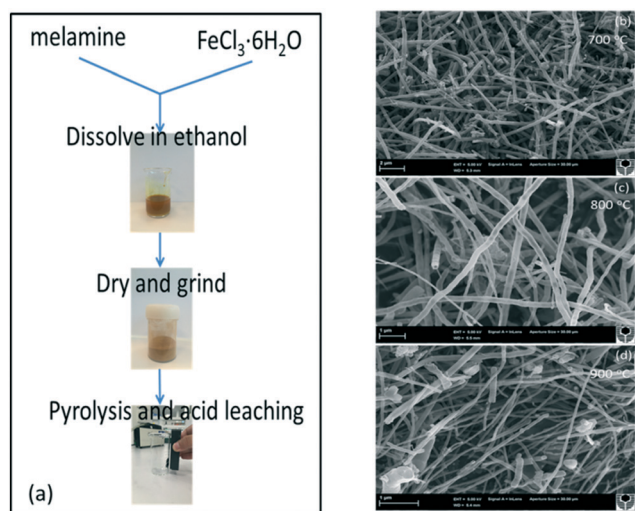

Fig. 1 (a) Schematic of the synthesis route of Fe$_3$C@NCNT. SEM images of the Fe$_3$C@NCNT catalysts at (b) 700 °C, (c) 800 °C and (d) 900 °C.
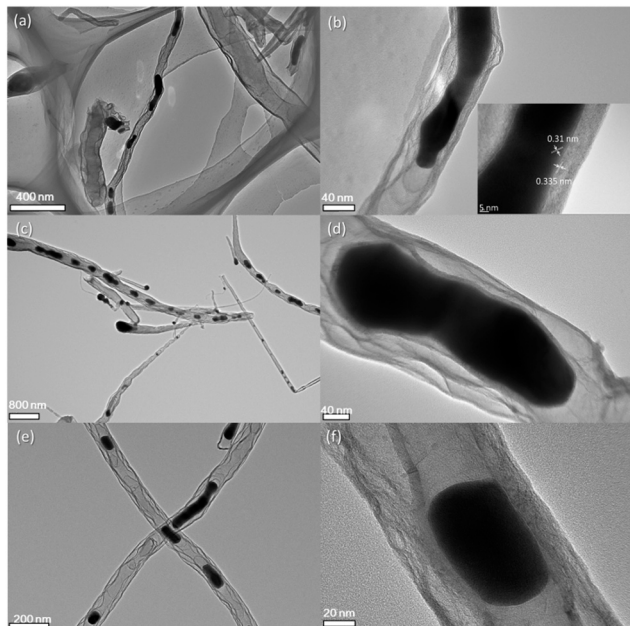
172 | *Environ. Sci.: Nano*, 2017, **4**, 170–179

This journal is © The Royal Society of Chemistry 2017

Fig. 2 TEM images of the Fe$_3$C@NCNT catalysts at 700 °C (a), (b), 800 °C (c), (d) and 900 °C (e), (f).

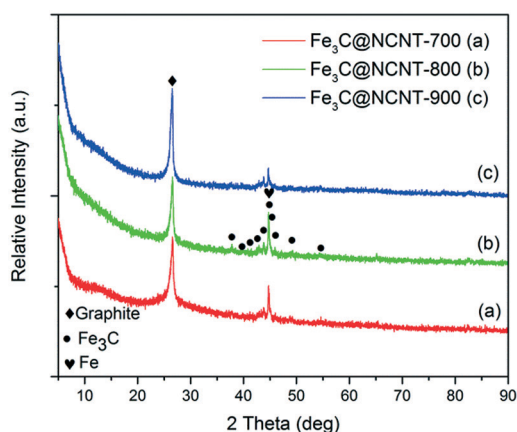**Fig. 3** XRD patterns of Fe$_3$C@NCNT composites at (a) 700 °C, (b) 800 °C and (c) 900 °C.

results for free-standing few-layer graphene.[26] Because of the protection of the graphitic layers, the Fe$_3$C nanocrystals were inaccessible and chemically stable in hot acids, implying that geometric confinement of Fe$_3$C@NCNT was successfully achieved.[26–28,41] Structure control is a continually difficult task for catalysts and materials prepared by pyrolysis. This is especially true for the synthesis and preparation of Fe$_3$C-based catalysts by pyrolysis. As far as we know, there are few reports of Fe$_3$C with uniform morphology and evenly dispersed nanoparticles.

X-ray diffraction (XRD) patterns of Fe$_3$C@NCNT obtained at different pyrolysis temperatures are shown in Fig. 3. The diffraction peaks at 26.5° and 43.4° were observed at different calcined temperatures, corresponding to the (002) and

(101) planes of graphitic carbon, respectively.[6] The diffraction peaks were very sharp and the intensity of the diffraction peak at 26.5° increased with pyrolysis temperature, indicating that the degree of graphitization of Fe$_3$C@NCNT was very good and was also strongly dependent on the pyrolysis temperature. In addition to this reflection, other diffraction peaks at 37 to 50° were the typical diffraction peaks of Fe$_3$C; these could not be found in NG[6] and were the major difference between Fe$_3$C@NCNT and NG. Diffraction peaks located at 37.8, 42.8, 43.9, 45.0, 45.8 and 49.2° were detected in Fe$_3$C@NCNT; these can be assigned to the (021), (121), (210), (103), (211) and (113) crystalline planes of Fe$_3$C particles, respectively.[42] This confirmed that the nanoparticles encapsulated in the interior of the nanotubes observed by TEM were dominantly Fe$_3$C when the temperature was above 700 °C. These diffraction peaks were the highest and strongest in Fe$_3$C@NCNT-800. In addition, all the samples may contain traces of metallic iron, as it has the same characteristic peak as Fe$_3$C at a 2θ of 44.6°.[26,33] The XRD results further confirmed that the Fe$_3$C nanoparticles were encapsulated in graphitic layers which could not be removed in hot acid solution and were well preserved after the leaching process.

The degree of graphitization of the Fe$_3$C@NCNT samples was further investigated by Raman spectra, and the results are shown in Fig. 4. The G band (at 1350 cm^{-1}) shows the existence of sp^2-hybridized carbon atoms, and the D band (at 1570 cm^{-1}) provides evidence of defects such as disorders, edges and boundaries of the graphene.[40] I_D/I_G is the ratio of the integrated intensities of the D and G bands; this ratio decreased with increasing pyrolysis temperature. As can be seen from Fig. 4, the intensity ratios of the D- and G-bands (I_D/I_G) for Fe$_3$C@NCNT-700, Fe$_3$C@NCNT-800 and Fe$_3$C@NCNT-900 were 1.20, 1.17 and 1.12, respectively, which demonstrates that the degree of graphitization increased with the pyrolysis temperature. An ordered graphitic structure can be formed easily at a higher temperature; however, if the pyrolysis temperature is too high, irregular carbon nanostructures can be formed. The reason for this is that Fe$_3$C is temperature
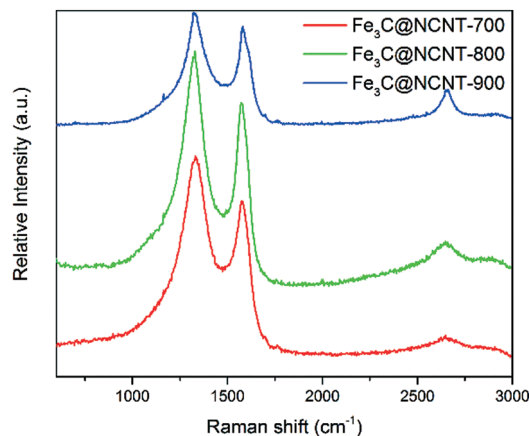

Fig. 4 Raman spectra of Fe$_3$C@NCNT composites at various pyrolysis temperatures.

This journal is © The Royal Society of Chemistry 2017

Environ. Sci.: Nano, 2017, **4**, 170–179 | 173

sensitive and metastable; at a higher temperature, it can break down into metallic Fe and free-C, which may enter the CNT framework and thus change its crystal structure.[28]

Fig. 5 displays the N_2 adsorption–desorption isotherms and pore size distributions of the $Fe_3C@NCNT$ samples. The isotherms in Fig. 5(a) show that N_2 adsorption increased with pyrolysis temperature; this is due to the higher surface areas and larger pore volumes at higher temperatures. All the samples exhibited typical IV isotherms with H3-type hysteresis loops. The hysteresis loops in $P/P_0 = 0.4$ to 0.9 were indicative of the mesoporous structures of the $Fe_3C@NCNT$ composites.[43]

The specific surface areas of $Fe_3C@NCNT$-700, Fe_3-$C@NCNT$-800 and $Fe_3C@NCNT$-900 were determined to be 40.1, 52.4 and 72.4 m² g⁻¹, respectively. Table 1 shows that the BET surface area and pore volume increased with increasing pyrolysis temperature; also, the pore size increased initially but then decreased, reaching its peak at 800 °C. The BET area increased; this indicates that high pyrolysis temperatures can break the CNTs into smaller pieces, thus resulting in the exposure of some Fe_3C nanoparticles, which may further increase the number of active sites and enhance the catalytic performance.
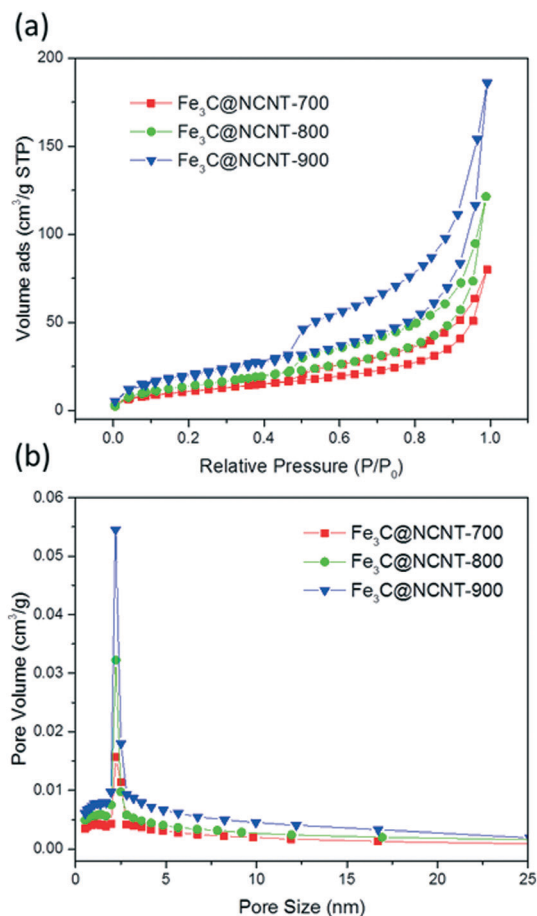
Table 1 BET surface area and pore properties of $Fe_3C@NCNT$ composites

	BET surface area, m² g⁻¹	Pore volume, cm³ g⁻¹	Average pore size, nm
$Fe_3C@NVNT$-700	40.1	0.096	6.1
$Fe_3C@NVNT$-800	52.4	0.15	6.7
$Fe_3C@NVNT$-900	72.4	0.23	6.5

Fig. 5(b) shows that all of the $Fe_3C@NCNT$ composites presented a single mode of pore size. The pore sizes of Fe_3-$C@NCNT$-700, $Fe_3C@NCNT$-800 and $Fe_3C@NCNT$-900 were centred at 6.1, 6.7 and 6.5 nm, which demonstrated that the pyrolysis temperature exerted little effect on the pore size.[44]

Fig. 6 shows the representative TGA and DTA curves of $Fe_3C@NCNT$ nanocomposites measured in air atmosphere from 25 to 1000 °C with a heating rate of 10 °C min⁻¹. The combustion temperature was found to be in the order Fe_3-$C@NCNT$-700 < $Fe_3C@NCNT$-800 < $Fe_3C@NCNT$-900.

The TGA plots of $Fe_3C@NCNT$ composites showed a slight weight increase below 250 °C followed by a mild weight loss from 250 °C to 450 °C, which can be assigned to the removal and destruction of the labile oxygenated functional groups on the carbon surface, such as –OH and C=O in the forms of H_2O, CO and CO_2.[45] Then, the weight decreased
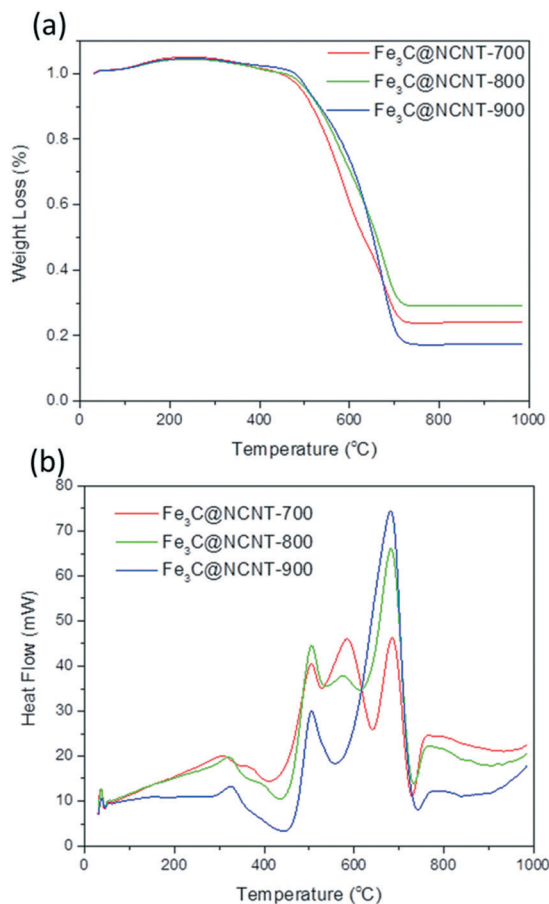

Fig. 5 (a) Nitrogen sorption isotherms of the samples and (b) pore size distributions calculated from N_2 desorption isotherms for $Fe_3C@NCNT$-700, $Fe_3C@NCNT$-800 and $Fe_3C@NCNT$-900.

Fig. 6 TGA (a) and DTA (b) curves of the $Fe_3C@NCNT$ composites.

174 | Environ. Sci.: Nano, 2017, 4, 170–179

This journal is © The Royal Society of Chemistry 2017

dramatically in the range from 450 °C to 700 °C, which was ascribed to the oxidation and decomposition of the CNTs and the oxidation and transformation of Fe_3C into Fe_2O_3 between 360 °C and 550 °C. When the temperature reached 700 °C, the weight of the samples remained unchanged, and almost no weight loss occurred beyond this temperature. Stable weight percentages of 24.25%, 29.30% and 17.54% (represents the weight of residual iron oxide yielding iron contents of 16.98%, 20.51% and 12.27% by calculation) were achieved for Fe$_3$C@NCNT-700, Fe$_3$C@NCNT-800 and Fe$_3$C@NCNT-900, respectively.[46] It is known that the weight loss rate of CNTs filled with ferromagnetic species always decreases with increasing temperature because of the destruction of the tube walls that provide protection to the inner filled metal, which results in the formation of metal oxides. It is deduced that a point of inflection would exist in the TGA curve. However, the curves of the Fe$_3$C@NCNT nanocomposites were relatively smooth, proving that the iron and iron carbide encapsulated inside the nanotubes were oxidized by air simultaneously with the tube walls.[47]

X-ray photoelectron spectra (XPS) studies were carried out to further investigate the nature of the surfaces of the Fe$_3$C@NCNT composites. Fig. 7(a) reveals that the Fe$_3$C@NCNT catalysts were composed of C, O, N, and Fe, and no impurity was observed. Although Fe was detected by ICP (Table S1†), TEM and XRD, the XPS spectra revealed low surface iron contents ($<0.2\%$) on all the Fe$_3$C@NCNT composites, implying complete leaching of surface iron species during the acid treatment. This further proves that the Fe$_3$C nanoparticles were entirely encapsulated by carbon layers in the catalysts and can thus survive the catalytic process. However, at a high temperature, carbon nanotubes may partially break up and crack (as shown by SEM); thus, the interior Fe$_3$C or Fe^0 may run out of the tubes. As a result, the iron content as analyzed by XPS in Fe$_3$C@NCNT-900 was the highest among all the catalysts.
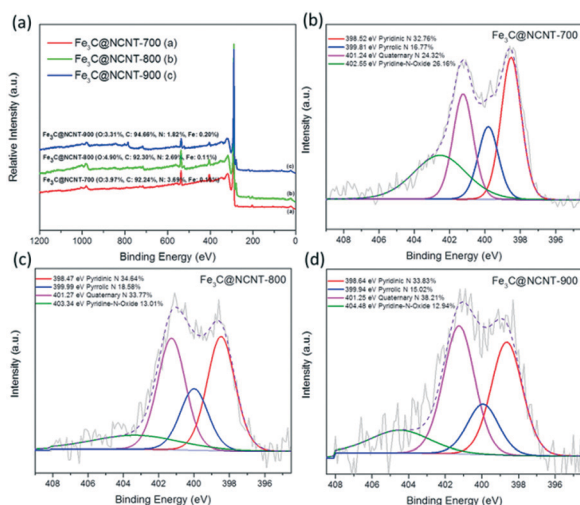
The total amount of surface N in the different catalysts was detected to be 3.69 at%, 2.69 at%, and 1.82 at% for Fe$_3$C@NCNT-700, Fe$_3$C@NCNT-800 and Fe$_3$C@NCNT-900, respectively. Meanwhile, the total amount of N detected by elemental analysis is shown in Table S2.† The decrease in total N content with increasing pyrolysis temperature may be ascribed to the decomposition of unstable nitrogen species at a high temperature. The N 1s spectra were deconvoluted into four peaks, assigned to pyridinic N (398.5 to 398.8 eV), pyrrolic N (399.9 to 400.2 eV), quaternary N (401.4 to 401.6 eV) and pyridine-N-oxide (402 to 405 eV),[48] as shown in Fig. 7(b)–(d). The content of quaternary N initially increased dramatically from 700 °C to 800 °C but then increased moderately from 800 °C to 900 °C. The content of pyridinic N demonstrated an inverse trend; it increased initially but then decreased with increasing pyrolysis temperature due to the loss of unstable N at higher temperatures. Pyridinic N is generally regarded to be connected with catalytic activity because it reduces the energy barrier for adsorbing reactants on adjacent carbon atoms and it accelerates first-electron transfer, which is limited by rate.[49,50] However, recent research has suggested that quaternary N in the graphene structure can cause nonuniform distribution of electrons, especially when two quaternary N atoms are doped into the same hexagon, leading to a dramatic improvement in the catalytic activity of the carbon surface.[28,51]

Catalytic performance and active site analysis

Control experiments were carried out to evaluate the adsorption, PMS self-oxidation and catalytic performance of Fe$_3$C@NCNT composites. The phenol removal results under different conditions are shown in Fig. 8(a). In the presence of PMS without catalyst, a negligible change (less than 6%) in phenol concentration was observed after 180 min, indicating
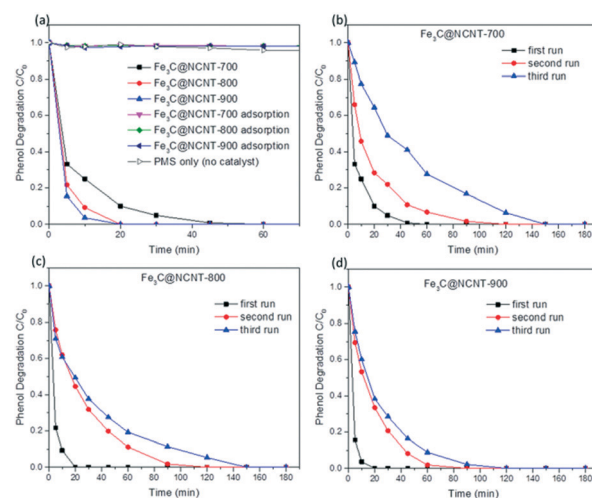

Fig. 7 (a) XPS spectra of Fe$_3$C@NCNT composites at different temperatures and HR XPS N 1s at (b) 700 °C, (c) 800 °C and (d) 900 °C.

Fig. 8 (a) Phenol removal under different conditions and stabilities of (b) Fe$_3$C@NCNT-700, (c) Fe$_3$C@NCNT-800 and (d) Fe$_3$C@NCNT-900. Reaction conditions: phenol 20 ppm, catalyst loading 0.2 g L^{-1}, PMS 2 g L^{-1}, temperature 25 °C.

This journal is © The Royal Society of Chemistry 2017

Environ. Sci.: Nano, 2017, **4**, 170–179 | 175

that significant phenol oxidation could not be induced by PMS itself. A similar trend was found in adsorption reactions with the Fe$_3$C@NCNT catalysts. Less than 2% phenol was removed in 180 min, suggesting that phenol adsorption on the Fe$_3$C@NCNT composites was also negligible.

As shown in Fig. 8(a), Fe$_3$C@NCNT-700, Fe$_3$C@NCNT-800 and Fe$_3$C@NCNT-900 can degrade 100% phenol in 45, 20 and 20 min, respectively. This efficiency is better than that of rGO,[11] N-doped graphene[6,52] and N-doped CNTs[14,35] and is exceptionally better than some metal-based carbon materials,[8,44,45] indicating that Fe$_3$C provides the active sites to accelerate this reaction. Fe$_3$C@NCNT-900 exhibited the best performance among all the Fe$_3$C@NCNT catalysts, implying that Fe$_3$C@NCNT-900, with wide CNTs that are open at both ends, was more accessible to enhance the phenol catalytic degradation reactions because the phenol molecules and Fe$_3$C were in full contact in a relatively restricted area.[28]

It is known that the stability of a catalyst is of great importance to its practical applications.[45] The stabilities and recyclabilities of the Fe$_3$C@NCNT catalysts were evaluated by successive tests of phenol degradation under the same reaction conditions. For Fe$_3$C@NCNT-700, 100% phenol was degraded within 45, 120, and 150 min for the first, second and third runs, respectively. For Fe$_3$C@NCNT-800, phenol removal was completed in 20, 120, and 150 min, respectively; Fe$_3$C@NCNT-900 required 20, 90, and 120 min, respectively. XRD patterns of Fe$_3$C@NCNT after the first run are shown in Fig. S3.† As can be seen, compared with the fresh sample, diffraction peaks of Fe$_2$O$_3$ appeared, suggesting that some Fe^0 was oxidized to Fe(III). Moreover, the peak intensity of Fe$_3$C decreased slightly for the recycled catalyst from the 1st run, suggesting that in addition to the oxidized Fe^0, some Fe$_3$C was consumed during the catalytic reaction.[25] Moreover, the intermediates formed from the oxidation processes may also block the active sites. Therefore, the results after the first, second and third runs were not as satisfactory as those of the fresh samples. The stability results were exceptionally better than those of N-doped graphene[6,52,53] and N-doped CNT,[14,35] implying that the inner stability of Fe$_3$C after the first run may play a role in the enhanced stability of the catalyst. The stability of Fe$_3$@NCNT-900 was relatively better because the carbon nanotubes and iron carbide were in close integration; the active sites decreased relatively little after three successive reactions, and the Fe$_3$C in the third run was still sufficient to activate the surrounding graphitic layers, consequently activating the outer surface of the carbon layer.[25]

In the heterogeneous catalytic oxidation of phenol, reaction parameters such as catalyst loading and reaction temperature can affect the phenol degradation rate. The effect of catalyst loading on the phenol degradation efficiency is shown in Fig. 9(a). The catalyst concentration exerted a significant influence on the phenol degradation efficiency, which was dramatically enhanced with an increase in the catalyst concentration. When the catalyst concentration was 0.1 g L^{-1}, 98% and 99% phenol were degraded in 180 min on Fe$_3$C@NCNT-700 and Fe$_3$C@NCNT-800, respectively, and
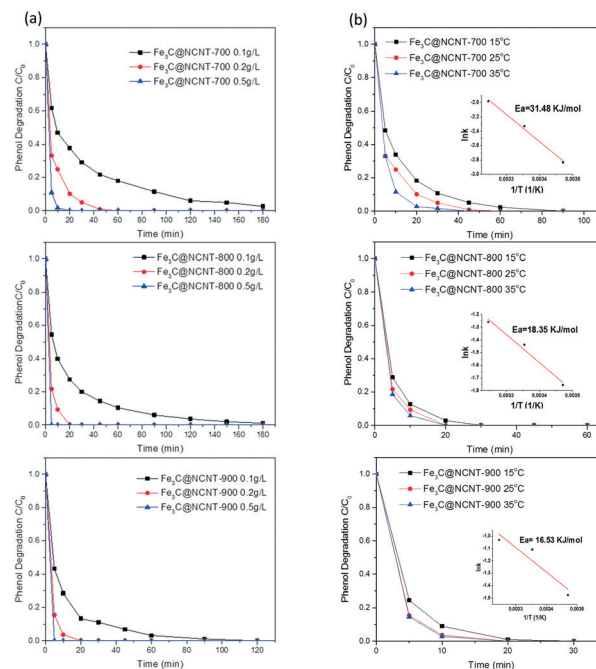

Fig. 9 Effects of (a) catalyst loading and (b) reaction temperature on phenol degradation for different Fe$_3$C@NCNT catalysts. Reaction conditions: phenol 20 ppm, PMS 2 g L^{-1}.

100% phenol was degraded in 120 min on Fe$_3$C@NCNT-900. When the catalyst concentration was increased to 0.5 g L^{-1}, phenol was completely removed after 30, 5 and 5 min on Fe$_3$C@NCNT-700, Fe$_3$C@NCNT-800 and Fe$_3$C@NCNT-900, respectively. The improvement in efficiency was attributed to the increase in the active sites of the reaction in the phenol solution, which generated more active radicals.

Fig. 9(b) shows the phenol degradation performance of the Fe$_3$C@NCNT catalysts at different reaction temperatures. It can be seen that the reaction temperature moderately affected the oxidation efficiency and degradation rate for Fe$_3$C@NCNT-700. However, for Fe$_3$C@NCNT-800 and Fe$_3$C@NCNT-900, the effect was relatively small. Specifically, at 15 °C, phenol degradation reached 100% in 90 min for Fe$_3$C@NCNT-700, while the times decreased to 60 and 45 min when the reaction temperature was increased to 25 °C and 35 °C, respectively. The kinetics of phenol degradation was evaluated by the first-order kinetic model, as listed below:

$$\ln(C/C_0) = -kt \qquad (1)$$

where C and C_0 are the phenol concentrations at time (t) and $t = 0$, respectively, and k is the reaction rate constant.[52]

The reaction rate constants (k) of phenol oxidation at 25 °C on Fe$_3$C@NCNT-700, Fe$_3$C@NCNT-800 and Fe$_3$C@NCNT-900 were then calculated to be 0.097, 0.237 and 0.330 min^{-1}, respectively.
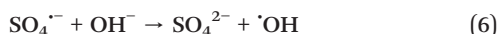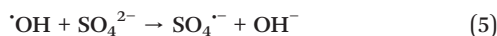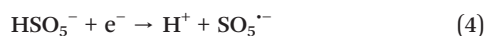
Based on first-order kinetics, the rate constants at varying temperatures were obtained, and the relationship was found

176 | *Environ. Sci.: Nano*, 2017, **4**, 170–179

This journal is © The Royal Society of Chemistry 2017

to follow the Arrhenius equation. The activation energy was thus obtained as 31.5 kJ mol^{-1} for Fe$_3$C@NCNT-700. For Fe$_3$-C@NCNT-800 and Fe$_3$C@NCNT-900, the degradation time decreased from 30 min to 20 min when the temperature increased from 15 to 35 °C. Also, the activation energies were 18.3 and 16.5 kJ mol^{-1}, respectively; these are much lower than the activation energies of N-doped graphene[6] and N-doped CNT.[35]

The mechanism of phenol degradation on Fe$_3$C@NCNT composites

The mechanisms of catalytic degradation of phenol on metal-based catalysts and carbon-based catalysts have recently been well investigated. Previous studies proved that these catalysts can activate PMS to produce sulfate and hydroxyl radicals.[7,12,35,52,54] As shown in Fig. S4,† Fe$_3$C@NCNT composites were able to effectively activate PMS to generate both ˙OH and SO$_4$˙$^-$. Different radical quenching reactions were also performed to probe the radicals produced in the Fe$_3$-C@NCNT composites and the contribution of the reactive species to phenol degradation. The reactions referring to the electron transfer processes facilitated by Fe$_3$C@NCNT are shown below.

$$HSO_5^- + e^- \rightarrow \,^{\bullet}OH + SO_4^{2-} \tag{2}$$

$$HSO_5^- + e^- \rightarrow \,^{\bullet}OH + SO_4^{\bullet-} \tag{3}$$

$$HSO_5^- + e^- \rightarrow H^+ + SO_5^{\bullet-} \tag{4}$$

$$^{\bullet}OH + SO_4^{2-} \rightarrow SO_4^{\bullet-} + OH^- \tag{5}$$

$$SO_4^{\bullet-} + OH^- \rightarrow SO_4^{2-} + \,^{\bullet}OH \tag{6}$$

Owing to its rapid reaction with both ˙OH and SO$_4$˙$^-$ radicals, ethanol was employed as an effective scavenger for both ˙OH and SO$_4$˙$^-$ radicals in the catalytic phenol degradation reactions. In most AOPs, radicals are critical to the organic degradation process. Therefore, if the quenching agent of ethanol is present in solution, the degradation will be significantly reduced or prevented.[35] Control experiments were conducted to compare the catalytic performance with the addition of ethanol on Fe$_3$C@NCNT-700, Fe$_3$C@NCNT-800 and Fe$_3$C@NCNT-900. As shown in Fig. 10(a), (c) and (e), all of the three catalysts maintained excellent phenol degradation performance, even with a high concentration of quenching reagent. Specifically, when ethanol was added at a molar ratio of 500 : 1 (ethanol : PMS), 100% phenol was degraded in 120, 45 and 45 min over Fe$_3$C@NCNT-700, Fe$_3$-C@NCNT-800 and Fe$_3$C@NCNT-900, respectively. Even in complete ethanol solution, 100% phenol was degraded in 180, 90 and 60 min, respectively. Although degradation still occurred with the quenching agent, which indicated that radical processes existed in this reaction, the results strongly suggested that generated ˙OH and SO$_4$˙$^-$ radicals played a relatively small role in phenol degradation, and other radicals or
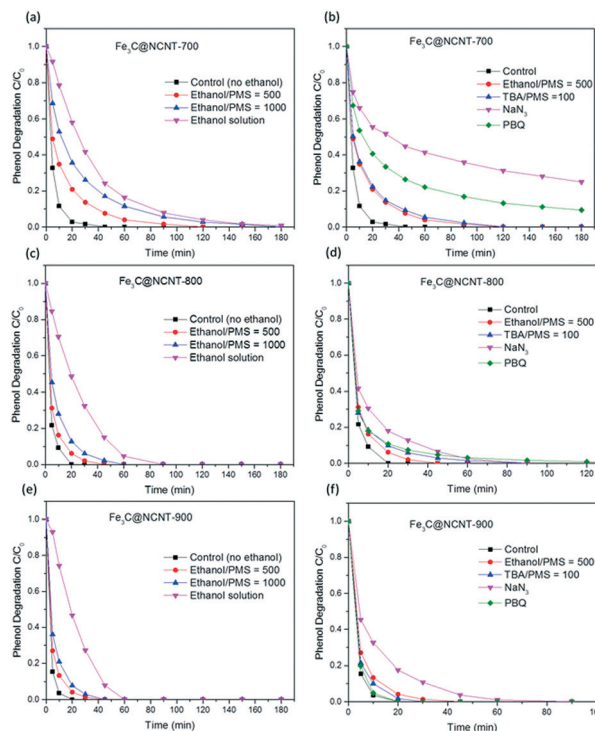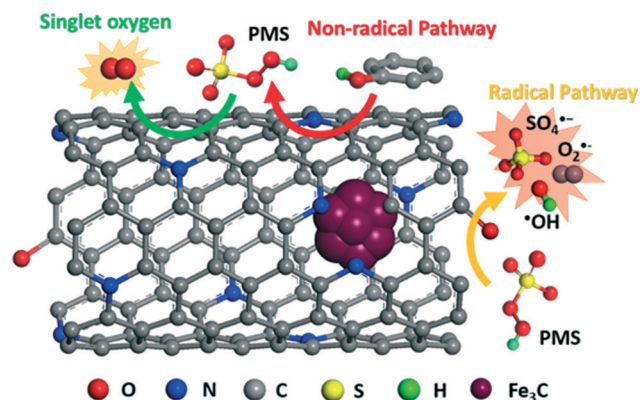

Fig. 10 Effects of radical quenching by ethanol on phenol degradation for (a) Fe$_3$C@NCNT-700, (c) Fe$_3$C@NCNT-800, and (e) Fe$_3$C@NCNT-900. Competitive radical tests for catalytic phenol degradation for (b) Fe$_3$C@NCNT-700, (d) Fe$_3$C@NCNT-800 and (f) Fe$_3$C@NCNT-900. Reaction conditions: phenol 20 ppm, catalyst loading 0.2 g L^{-1}, PMS 2 g L^{-1}, temperature 25 °C.

non-radical processes may play more significant roles. Due to the instantaneous reaction with hydroxyl radicals and the stagnated reaction with sulfate radicals, *tert*-butanol (TBA) was suggested to be an effective scavenger for ˙OH in the catalytic oxidation process.[55] When TBA was added to the reaction solution at a molar ratio of 100 : 1 (TBA : PMS), 100% phenol was degraded in 120, 90 and 30 min on Fe$_3$C@NCNT-700, Fe$_3$C@NCNT-800 and Fe$_3$C@NCNT-900. The degradation efficiency was not significantly reduced or prevented by the addition of ethanol or TBA; thus, we can conclude that both ˙OH and SO$_4$˙$^-$ radicals were not the dominant reactive species for these catalytic oxidation processes but that SO$_4$˙$^-$ made a larger contribution than ˙OH to phenol degradation.

Previous studies have demonstrated that singlet oxygen (^{1}O$_2$) is also generated from the catalytic oxidation process. Sodium azide (NaN$_3$) is an effective quenching agent for ^{1}O$_2$; however, it also reacts rapidly with ˙OH.[56–58] However, ˙OH was proved to be inactive for phenol decomposition in the above ethanol quenching experiment. In this process, 3 mM NaN$_3$ was added to the catalytic reaction solution. Although some of the NaN$_3$ was consumed by PMS, the remaining NaN$_3$ was sufficient to quench free radicals. It was found that the phenol degradation efficiency dramatically decreased with the addition of NaN$_3$; only 75% phenol was degraded in 180 min on Fe$_3$C@NCNT-700, and 100% phenol was degraded in almost 90 min on both Fe$_3$C@NCNT-800 and

This journal is © The Royal Society of Chemistry 2017

Environ. Sci.: Nano, 2017, **4**, 170–179 | 177

Scheme 1 Proposed mechanism of PMS activation on $Fe_3C@NCNT$.

Fe$_3$C@NCNT-900. These results suggest that $^1O_2$ is the major reactive species in phenol degradation.

The contribution of $\cdot O_2^-$ in phenol degradation was determined using *p*-benzoquinone (PBQ), an effective quenching agent for $\cdot O_2^-$.[59,60] When 3 mM PBQ was placed in the catalytic phenol solution, it was observed that 90.6% phenol was degraded in 180 min over Fe$_3$C@NCNT-700, 100% phenol was degraded in almost 180 min over Fe$_3$C@NCNT-800 and 100% phenol was degraded in 20 min over Fe$_3$C@NCNT-900. The phenol degradation efficiency was suppressed greatly by the addition of PBQ for Fe$_3$C@NCNT-700 and Fe$_3$C@NCNT-800, but did not change for Fe$_3$C@NCNT-900, revealing that $\cdot O_2^-$ was responsible for phenol decomposition for the former two catalysts. This may be because of the breakup of CNTs at high temperature, leading to the exposure of some Fe$_3$C nanoparticles and thus reducing the generation of $\cdot O_2^-$. A proposed mechanism of PMS activation on Fe$_3$C@NCNT is illustrated in Scheme 1.

Overall, in the above four scavenging tests, $^1O_2$ and $\cdot O_2^-$ were recognized as the dominant reactive oxygen species generated in phenol catalytic degradation on Fe$_3$C@NCNT-700 and Fe$_3$C@NCNT-800; $^1O_2$ exhibited a larger contribution. However, for Fe$_3$C@NCNT-900, only $^1O_2$ was recognized as the major reactive oxygen species. For all of the three catalysts, both $\cdot OH$ and $SO_4^{\cdot-}$ exerted very small impacts on phenol degradation.[61] Therefore, in this investigation, the possible mechanism of the superior activity and excellent stability of Fe$_3$C@NCNT catalysts in the activation of PMS for phenol degradation can be explained by a combination of radical and nonradical processes, which were significantly promoted by quaternary and pyridinic N, and by synergetic effects between the inner Fe$_3$C and outside carbon as well as by trace amounts of Fe on the surface.

Conclusions

In summary, nitrogen-doped carbon nanotubes with encapsulated Fe$_3$C nanoparticles (Fe$_3$C@NCNT) were successfully prepared through a simple and green pyrolysis process of melamine and iron chlorides. The characterization results showed that Fe$_3$C nanocrystals were mainly encapsulated in the interior of the Fe$_3$C@NCNT composites. The as-prepared Fe$_3$-C@NCNT catalysts exhibited both excellent catalytic performance and outstanding stability in phenol degradation. The quaternary and pyridinic N, synergetic effects between the inner Fe$_3$C and outside carbon, and trace amounts of Fe on the surface may be the active sites to enhance catalytic degradation. Quenching experiments were used to observe the generated reactive radicals, and $^1O_2$ and $\cdot O_2^-$ were proven to be the major radicals in catalytic phenol degradation. This novel synthetic approach, unique structure and proposed mechanism will stimulate the development of active and durable metal-based carbon catalysts in environmental science research.

Notes and references

1 F. Perreault, A. Fonseca de Faria and M. Elimelech, *Chem. Soc. Rev.*, 2015, **44**, 5861–5896.
2 X. G. Duan, Z. M. Ao, L. Zhou, H. Q. Sun, G. X. Wang and S. B. Wang, *Appl. Catal., B*, 2016, **188**, 98–105.
3 X. G. Duan, C. Su, L. Zhou, H. Q. Sun, A. Suvorova, T. Odedairo, Z. H. Zhu, Z. P. Shao and S. B. Wang, *Appl. Catal., B*, 2016, **194**, 7–15.
4 J. Kang, X. G. Duan, L. Zhou, H. Q. Sun, M. O. Tade and S. B. Wang, *Chem. Eng. J.*, 2016, **288**, 399–405.
5 W. J. Tian, H. Y. Zhang, X. G. Duan, H. Q. Sun, M. O. Tade, H. M. Ang and S. B. Wang, *ACS Appl. Mater. Interfaces*, 2016, **8**, 7184–7193.
6 C. Wang, J. Kang, H. Q. Sun, H. M. Ang, M. O. Tade and S. B. Wang, *Carbon*, 2016, **102**, 279–287.
7 Y. Wang, S. Indrawirawan, X. Duan, H. Sun, H. M. Ang, M. O. Tadé and S. Wang, *Chem. Eng. J.*, 2015, **266**, 12–20.
8 Y. Wang, H. Sun, H. M. Ang, M. O. Tadé and S. Wang, *J. Colloid Interface Sci.*, 2014, **433**, 68–75.
9 Y. Wang, H. Sun, H. M. Ang, M. O. Tadé and S. Wang, *Appl. Catal., B*, 2015, **164**, 159–167.
10 Y. J. Yao, Y. M. Cai, G. D. Wu, F. Y. Wei, X. Y. Li, H. Chen and S. B. Wang, *J. Hazard. Mater.*, 2015, **296**, 128–137.
11 H. Sun, S. Liu, G. Zhou, H. M. Ang, M. O. Tadé and S. Wang, *ACS Appl. Mater. Interfaces*, 2012, **4**, 5466–5471.
12 X. Duan, H. Sun, J. Kang, Y. Wang, S. Indrawirawan and S. Wang, *ACS Catal.*, 2015, **5**, 4629–4636.

178 | *Environ. Sci.: Nano*, 2017, **4**, 170–179

This journal is © The Royal Society of Chemistry 2017

13 H. Sun, Y. Wang, S. Liu, L. Ge, L. Wang, Z. Zhu and S. Wang, *Chem. Commun.*, 2013, **49**, 9914–9916.

14 H. Q. Sun, C. Kwan, A. Suvorova, H. M. Ang, M. O. Tade and S. B. Wang, *Appl. Catal., B*, 2014, **154**, 134–141.

15 M. Lefevre, E. Proietti, F. Jaouen and J. P. Dodelet, *Science*, 2009, **324**, 71–74.

16 Z. Chen, D. Higgins, A. Yu, L. Zhang and J. Zhang, *Energy Environ. Sci.*, 2011, **4**, 3167–3192.

17 Z. Y. Wu, X. X. Xu, B. C. Hu, H. W. Liang, Y. Lin, L. F. Chen and S. H. Yu, *Angew. Chem., Int. Ed.*, 2015, **54**, 8179–8183.

18 Z. W. Chen, D. Higgins, A. P. Yu, L. Zhang and J. J. Zhang, *Energy Environ. Sci.*, 2011, **4**, 3167–3192.

19 X. G. Li, G. Liu and B. N. Popov, *J. Power Sources*, 2010, **195**, 6373–6378.

20 F. Jaouen, E. Proietti, M. Lefevre, R. Chenitz, J. P. Dodelet, G. Wu, H. T. Chung, C. M. Johnston and P. Zelenay, *Energy Environ. Sci.*, 2011, **4**, 114–130.

21 T. Yang and G. Q. Han, *Int. J. Electrochem. Sci.*, 2012, **7**, 10884–10893.

22 H. J. Zhang, Q. Z. Jiang, L. L. Sun, X. X. Yuan, Z. P. Shao and Z. F. Ma, *Int. J. Hydrogen Energy*, 2010, **35**, 8295–8302.

23 D. H. Deng, L. Yu, X. Q. Chen, G. X. Wang, L. Jin, X. L. Pan, J. Deng, G. Q. Sun and X. H. Bao, *Angew. Chem., Int. Ed.*, 2013, **52**, 371–375.

24 Y. Hu, J. O. Jensen, W. Zhang, L. N. Cleemann, W. Xing, N. J. Bjerrum and Q. F. Li, *Angew. Chem., Int. Ed.*, 2014, **53**, 3675–3679.

25 Y. Wang, H. Sun, X. Duan, H. M. Ang, M. O. Tadé and S. Wang, *Appl. Catal., B*, 2015, **172–173**, 73–81.

26 G. Zhong, H. Wang, H. Yu and F. Peng, *J. Power Sources*, 2015, **286**, 495–503.

27 Y. J. Yao, H. Chen, C. Lian, F. Y. Wei, D. W. Zhang, G. D. Wu, B. J. Chen and S. B. Wang, *J. Hazard. Mater.*, 2016, **314**, 129–139.

28 J. J. Shi, Y. Y. Wang, W. C. Du and Z. Y. Hou, *Carbon*, 2016, **99**, 330–337.

29 M. Li, Y. P. Xiong, X. T. Liu, C. Han, Y. F. Zhang, X. J. Bo and L. P. Guo, *J. Mater. Chem. A*, 2015, **3**, 9658–9667.

30 W. X. Yang, X. J. Liu, X. Y. Yue, J. B. Jia and S. J. Guo, *J. Am. Chem. Soc.*, 2015, **137**, 1436–1439.

31 W. Wei, H. W. Liang, K. Parvez, X. D. Zhuang, X. L. Feng and K. Mullen, *Angew. Chem., Int. Ed.*, 2014, **53**, 1570–1574.

32 S. Trasobares, O. Stephan, C. Colliex, W. K. Hsu, H. W. Kroto and D. R. M. Walton, *J. Chem. Phys.*, 2002, **116**, 8966–8972.

33 A. B. Wu, D. M. Liu, L. Z. Tong, L. X. Yu and H. Yang, *CrystEngComm*, 2011, **13**, 876–882.

34 V. Nallathambi, N. Leonard, R. Kothandaraman and S. C. Barton, *Electrochem. Solid-State Lett.*, 2011, **14**, B55–B58.

35 X. Duan, H. Sun, Y. Wang, J. Kang and S. Wang, *ACS Catal.*, 2015, **5**, 553–559.

36 A. K. Schaper, H. Q. Hou, A. Greiner and F. Phillipp, *J. Catal.*, 2004, **222**, 250–254.

37 J. Y. Liang, C. C. Wang and S. Y. Lu, *J. Mater. Chem. A*, 2015, **3**, 24453–24462.

38 S. M. Zhang, H. Y. Zhang, Q. Liu and S. L. Chen, *J. Mater. Chem. A*, 2013, **1**, 3302–3308.

39 H. Kim and W. Sigmund, *Carbon*, 2005, **43**, 1743–1748.

40 B. Zhang, J. Song, G. Yang and B. Han, *Chem. Sci.*, 2014, **5**, 4656–4660.

41 Y. Yao, H. Chen, J. Qin, G. Wu, C. Lian, J. Zhang and S. Wang, *Water Res.*, 2016, **101**, 281–291.

42 M. Zhao and H. H. Song, *Mater. Chem. Phys.*, 2010, **124**, 861–864.

43 Y. Z. Wang, Y. Liu, W. Liu, H. Y. Chen, G. X. Zhang and J. H. Wang, *Mater. Lett.*, 2015, **154**, 64–67.

44 Y. Wang, H. Sun, H. M. Ang, M. O. Tadé and S. Wang, *ACS Appl. Mater. Interfaces*, 2014, **6**, 19914–19923.

45 Y. Wang, H. Sun, H. M. Ang, M. O. Tadé and S. Wang, *Chem. Eng. J.*, 2014, **245**, 1–9.

46 J. Zhang, R. Wang, E. Z. Liu, X. F. Gao, Z. H. Sun, F. S. Xiao, F. Girgsdies and D. S. Su, *Angew. Chem., Int. Ed.*, 2012, **51**, 7581–7585.

47 Y. Liu, X. Z. Wang, Y. F. Dong, Z. Y. Wang, Z. B. Zhao and J. S. Qiu, *J. Mater. Chem. A*, 2014, **2**, 16832–16835.

48 S. Kundu, W. Xia, W. Busser, M. Becker, D. A. Schmidt, M. Havenith and M. Muhler, *Phys. Chem. Chem. Phys.*, 2010, **12**, 4351–4359.

49 O. Soares, R. P. Rocha, A. G. Goncalves, J. L. Figueiredo, J. J. M. Orfao and M. F. R. Pereira, *Carbon*, 2015, **91**, 114–121.

50 G. Wu, K. L. More, P. Xu, H. L. Wang, M. Ferrandon, A. J. Kropf, D. J. Myers, S. G. Ma, C. M. Johnston and P. Zelenay, *Chem. Commun.*, 2013, **49**, 3291–3293.

51 M. L. Xiao, J. B. Zhu, L. G. Feng, C. P. Liu and W. Xing, *Adv. Mater.*, 2015, **27**, 2521–2527.

52 X. Duan, Z. Ao, H. Sun, S. Indrawirawan, Y. Wang, J. Kang, F. Liang, Z. H. Zhu and S. Wang, *ACS Appl. Mater. Interfaces*, 2015, **7**, 4169–4178.

53 X. Duan, K. O'Donnell, H. Sun, Y. Wang and S. Wang, *Small*, 2015, **11**, 3036–3044.

54 B. Jiang, D. Dai, Y. Yao, T. Xu, R. Li, R. Xie, L. Chen and W. Chen, *Chem. Commun.*, 2016, **52**, 9566–9569.

55 H. Zhao, Y. M. Dong, P. P. Jiang, G. L. Wang, J. J. Zhang, K. Li and C. Y. Feng, *New J. Chem.*, 2014, **38**, 1743–1750.

56 A. Jawad, X. Y. Lu, Z. Q. Chen and G. C. Yin, *J. Phys. Chem. A*, 2014, **118**, 10028–10035.

57 J. Catalan, C. Diaz and L. Barrio, *Chem. Phys.*, 2004, **300**, 33–39.

58 R. A. Lundeen, C. H. Chu, M. Sander and K. McNeill, *Environ. Sci. Technol.*, 2016, **50**, 8586–8595.

59 M. Q. Yang, Y. H. Zhang, N. Zhang, Z. R. Tang and Y. J. Xu, *Sci. Rep.*, 2013, **3**, 3314.

60 Y. Zhou, J. Jiang, Y. Gao, J. Ma, S. Y. Pang, J. Li, X. T. Lu and L. P. Yuan, *Environ. Sci. Technol.*, 2015, **49**, 12941–12950.

61 Y. X. Wang, Y. B. Xie, H. Q. Sun, J. D. Xiao, H. B. Cao and S. B. Wang, *ACS Appl. Mater. Interfaces*, 2016, **8**, 9710–9720.

This journal is © The Royal Society of Chemistry 2017

Environ. Sci.: Nano, 2017, **4**, 170–179 | 179